

A New Proposal to Jefferson Lab PAC48

Measurement of the Two-Photon Exchange contribution to the electron-neutron elastic scattering cross section

S. Alsalmi (spokesperson)

King Saud University, Riyadh 11451, Saudi Arabia

E. Fuchey (spokesperson) and A.J.R. Puckett

University of Connecticut, Storrs, Connecticut 06269, USA

B. Wojtsekhowski (spokesperson), S. Barcus, A. Camsonne*, J-P. Chen*,

D. Gaskell, O. Hansen, D. W. Higinbotham, M. Jones, C. Keppel*, D. Mack,

D. Meekins, R. Michaels, B. Sawatzky, G. Smith, A. Tadepalli, and S. Wood

Thomas Jefferson National Accelerator Facility, Newport News, Virginia 23606, USA

K. Aniol

California State University, Los Angeles, CA 90032, USA

J. Arrington and P. Reimer

Argonne National Laboratory, 9700 S Cass Ave, Lemont, Illinois 60439, USA

T. Averett

The College of William and Mary, Williamsburg, Virginia 23185, USA

J. Bernauer

Stony Brook University, Stony Brook, NY 11794, US

Riken BNL Research Center, Upton, NY 11973, US

W. Boeglin and P. Markowitz

Florida International University, Miami, FL 33199, USA

G. Cates*, K. Gnanvo, C. Gu*, J. Liu*, N. Liyanage, V. Nelyubin, and C. Palatchi*

University of Virginia, Charlottesville, Virginia 232904, USA

M.E. Christy, B. Dongwi, I. Fernando, T. Gautam,

M. Kohl, J. Nazeer, T. Patel, and M. Rathnayake

Hampton University, Hampton, Virginia 23669, USA

E. Cline

Stony Brook University, Stony Brook, NY 11794, US

E. Cisbani, F. Meddi*, and G. Urciuoli*

Istituto Nazionale di Fisica Nucleare - Sezione di Roma,

P.le Aldo Moro, 2 - 00185 Roma, Italy

J.C. Cornejo* and B. Quinn*

Carnegie Mellon University, Pittsburgh, Pennsylvania 15213, USA

B. Crowe* and B. Vlahovic*

North Carolina Central University, Durham, North Carolina 27707, USA

C. Ayerbe Gayoso

Mississippi State University, Mississippi State, MS 39762, USA

D. Hamilton and R. Montgomery

SUPA School of Physics and Astronomy,

University of Glasgow, Glasgow G12 8QQ, UK

F. Hauenstein

Old Dominion University, Norfolk, Virginia 23529, USA

A. T. Katramatou and G.G. Petratos
Kent State University, Kent, OH 44242, USA

D. Nguyen
Massachusetts Institute of Technology, Cambridge, MA 02139, USA

C. Petta*
Istituto Nazionale di Fisica Nucleare, Dipt. di Fisica dell Univ. di Catania, I-95123 Catania, Italy

A. Sarty
Saint Mary's University, Halifax, Nova Scotia B3H 3C3, Canada

A. Schmidt
The George Washington University, Washington, DC 20052, USA

K. Slifer*
University of New Hampshire, Durham, NH 03824, USA

A. Shahinyan
AANL, 2 Alikhanian Brothers Street, 0036, Yerevan, Armenia

S. Širca*
Faculty of Mathematics and Physics, University of Ljubljana, 1000 Ljubljana, Slovenia

C. Sutera
Istituto Nazionale di Fisica Nucleare, Sezione di Catania, I-95123 Catania, Italy

W. Tireman
Northern Michigan University, Marquette, Michigan 49855, USA
(Dated: June 16, 2020)

(* - TBC)

Abstract

We propose to make a high precision measurement of the two-photon exchange contribution (TPE) in elastic electron-neutron scattering at a four-momentum transfer $Q^2 = 4.5$ $(\text{GeV}/c)^2$. While significant efforts to study the two-photon-exchange have focused around elastic electron-proton scattering, the impact of TPE on neutron form factors was never examined experimentally. The proposed experiment will provide the very first assessment of the two-photon exchange in electron-neutron scattering, which will be important for understanding the nucleon form factor physics.

The proposed experiment will be performed in Hall A using the BigBite (BB) spectrometer to detect the scattered electrons and the Super-BigBite (SBS) to detect the protons and neutrons. The experiment should run concurrently with the E12-09-019 G_M^n and E12-17-004 G_E^n -Recoil experiments, which are expected to run in 2021. The experimental setup of the proposed experiment will be identical to that of E12-09-019 experiment.

The “ratio” method will be used to extract the electric form factor of the neutron G_E^n by scattering unpolarized electrons from deuterium quasi-elastically at two beam energies 4.4 and 6.6 GeV and electron scattering angles 41.9 and 23.3 degrees respectively. In the proposed approach, systematic errors are greatly reduced compared to those in the traditional single electron arm configuration. Several experiments at Mainz and JLab have used the ratio method to measure the neutron magnetic form factor in the past years. The method can be extended to extract the neutron electric form factor even with less stringent requirements on the knowledge of the absolute neutron detection efficiency and experimental kinematics.

I. INTRODUCTION

In 1950's, a series of experiments performed by R. Hofstadter [1] revealed that the nucleons have a substructure (would be called later the quarks and gluons). The experiment confirmed M. Rosenbluth's theory [2] based on one-photon exchange approximation. In the Born approximation, where the interaction between the electron and the nucleon occurs *via* an exchange of a one virtual photon (OPE), the unpolarized $e - N$ elastic cross section can be expressed in terms of a nucleon magnetic, G_M , and electric, G_E , form factors. These form factors describe the deviation from a point-like scattering cross section:

$$\left(\frac{d\sigma}{d\Omega} \right)_{eN \rightarrow eN} = \frac{\sigma_{Mott}}{\epsilon(1 + \tau)} [\tau \cdot G_M^2(Q^2) + \epsilon \cdot G_E^2(Q^2)], \quad (1)$$

where E and E' are the incident and scattered electron energies, respectively, θ is the electron scattering angle, $\tau \equiv -q^2/4M^2$, with $-q^2 \equiv Q^2 = 4EE' \sin(\theta/2)$ being the negative four momentum transfer square, M is the nucleon mass, and $\epsilon = [1 + 2(1 + \tau) \tan^2(\theta/2)]^{-1}$ is the longitudinal polarization of the virtual photon. The reduced cross section is defined by:

$$\sigma_r \equiv \left(\frac{d\sigma}{d\Omega} \right) \cdot \frac{\epsilon(1 + \tau)}{\sigma_{Mott}} = \tau \cdot G_M^2(Q^2) + \epsilon \cdot G_E^2(Q^2) = \sigma_T + \epsilon \cdot \sigma_L, \quad (2)$$

where σ_L and σ_T are the cross sections for longitudinally and transversely polarized virtual photons, respectively.

The linear ϵ dependence of the cross section is due to σ_L term, see Eq. 1. The ratio σ_L/σ_T is a Rosenbluth slope related to G_E/G_M (in OPE), see Fig. 1. The data show that at Q^2 of 4-5 $(\text{GeV}/c)^2$ the Rosenbluth slope is three-four times larger than it suppose to be (in OPE) for the observed values of the G_E^p/G_M^p ratio.

The nucleon electromagnetic form factors can reveal a lot of information about the nucleon internal structure, as well as the quark distribution. The form factors depend only on one variable the negative square of the four-momentum transfer carried by the photon, Q^2 . In the limit of large Q^2 , pQCD provides well-motivated predictions for the Q^2 -dependance of



FIG. 1. The square root of Rosenbluth slope, corrected for kinematical factor $\sqrt{\tau}$ and μ_p , observed in elastic electron-proton scattering, adopted from Ref. [3].

the form factors and their ratio. However, it was never predicted at what Q^2 range the pQCD prediction (scaling) will be valid. Studies of GPDs show that pQCD validity will require a very large Q^2 of 100 (GeV/c)^2 . It was discovered at JLab, using the double polarization methods, that the proton electric and magnetic form factors behave differently starting at $Q^2 \approx 1 \text{ (GeV/c)}^2$.

Experimentally, the nucleon form factors can be measured using one of two techniques: polarization transfer technique and Rosenbluth technique. The polarization method examines the polarization transfer from longitudinally polarized electron to the recoiling nucleon and determine the resulting azimuthal asymmetry distribution using a polarimeter. Alternatively, one can use the polarized electron beam and a polarized target. While in the Rosenbluth method, the electric and magnetic form factors can be separated by making two or more measurements with different ϵ values (*i.e.* different beam energies and angles), but with same Q^2 value. Rosenbluth technique requires an accurate measurement of the cross section and suffers from large systematic uncertainties arising from several factors. For instance, an accurate knowledge of the neutron detector efficiency is required.

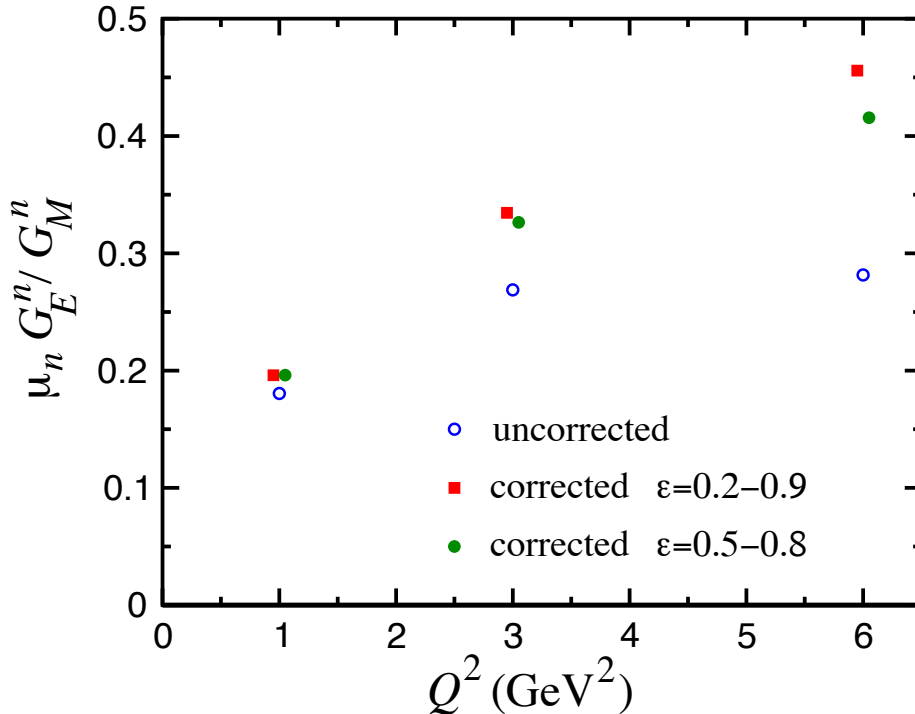


FIG. 2. Projected impact of TPE on G_E^n/G_M^n using LT separation, according to Ref. [4].

When comparing the values of G_E^n/G_M^n obtained from both techniques, a significant discrepancy was observed (see Fig. 1). Such discrepancy implies a potential problem in our understanding of the nucleon substructure. Many efforts were made in order to provide legitimate explanation, and it is believed that the inconsistency is due to contribution of two-photon exchange in $e - N$ elastic scattering process, see Refs. [5, 6]. Predictions made for the neutron case are shown in Fig. 2, adopted from [4]. The contribution of TPE could reach about 30% of Rosenbluth slope value at 5 (GeV/c) 2 .

In the following we propose to make precision L/T separation of the elastic electron-neutron cross section and first experimental assessment of the two-photon exchange contribution on the neutron magnetic form factor measurements (see also Ref. [7]). The result of the nTPE experiment will likely add a new component to our understanding of the elastic

⁵⁰ electron-nucleon process.

51

II. PHYSICS MOTIVATION

52 The nucleon plays the same central role in hadronic physics that the hydrogen atom does
 53 in atomic physics and the deuteron in the physics of nuclei. The structure of the nucleon
 54 and its specific properties, such as charge, magnetic moment, size, mass; the elastic electron
 55 scattering form factors, resonances; and structure functions in DIS, are of fundamental sci-
 56 entific interest. The isospin is a fundamental property of the nucleon, so both the proton and
 57 neutron investigations are important to do. By using data on the proton and neutron form
 58 factors the flavour structure could be explored [8]. It is already provided the most direct
 59 evidence for a diquark correlation in the nucleon [9–11].

60 Hadron structure, as seen in elastic electron scattering, in one-photon approximation,
 61 defined by two functions of four momentum transfer square. They are: the helicity conserving
 62 Dirac form factor, F_1 , which describes the distribution of the electric charge, and the helicity
 63 non-conserving Pauli form factor, F_2 , describes the distribution of the magnetic moment.
 64 These two form factors are the ingredients of the hadronic current. These form factors
 65 contain information on the transverse charge distribution for an unpolarized and transversely
 66 polarized nucleon, respectively, in the infinite momentum frame [12, 13].

67 The Sachs form factors, G_E and G_M , the ratio of which will be extracted directly from
 68 the data, are related to F_1 and F_2 by

$$F_1 = \frac{G_E + \tau G_M}{1 + \tau} \text{ and } F_2 = \frac{G_M - G_E}{\kappa(1 + \tau)}, \quad (3)$$

69 where κ is the nucleon anomalous magnetic moment.

70 Already twenty four years ago, important developments in QCD phenomenology has
 71 been the exploration of the generalized parton distribution (GPD) formalism [14–16], which
 72 provides relations between inclusive and exclusive observables. The nucleon elastic form
 73 factors F_1 and F_2 are given by the first moments of the GPDs

$$F_1(t) = \sum_q \int_0^1 H^q(x, \xi, t, \mu) dx \text{ and } F_2(t) = \sum_q \int_0^1 E^q(x, \xi, t, \mu) dx, \quad (4)$$

74 where H^q and E^q are two of the generalized parton distributions, x is the standard Bjorken
 75 x , ξ is the “skewness” of the reaction, t is the four-momentum transferred by the electron,

⁷⁶ μ is a scale parameter necessary from the evolution over Q^2 , analogous to DIS parton dis-
⁷⁷ tributions, and the sum is over all quarks and anti-quarks. These may be accessed through
⁷⁸ processes such as deeply virtual Compton scattering, where the interaction is factorized into
⁷⁹ a hard part with the virtual photon/photon interactions with an individual quark and a soft
⁸⁰ part of the residual system where the GPD information is contained.

⁸¹ Fundamental nucleon feature, the spin, is related to GPDs, as shown by X. Ji [15]. The
⁸² moments of GPDs can yield information, according to the Ji's Angular Momentum Sum
⁸³ Rule, on the contribution to the nucleon spin from quarks and gluons, including both the
⁸⁴ quark spin and orbital angular momentum.

⁸⁵ At present, experimental measurements of GPDs are still scarce. Until high Q^2 DVCS
⁸⁶ data becomes available, work has been done to attempt to parameterize these GPDs, which
⁸⁷ rely heavily on data from electromagnetic form factors and parton distributions from DIS as
⁸⁸ constraints [17]. Data at high Q^2 for G_E^n would contribute significantly in the development
⁸⁹ of these models.

⁹⁰ As we presented above the form factors are important components for GPDs development.
⁹¹ However, the cross section of elastic $e-p$ scattering contains a significant contribution to σ_L ,
⁹² which at high Q^2 is much larger than theory calculations expected [18]. Such an alarming
⁹³ observation underlines that understanding of TPE effect is essential for hadron physics.

94

III. TECHNIQUE

95 This proposal is based on instrumentation, simulation, and analysis development made
 96 by the GMn/SBS collaboration for the GMn, E12-09-019, experiment [19]. The GMn experi-
 97 ment is one of several form factor experiments approved by JLab PAC. The SBS spectrometer
 98 was funded by DOE with large contributions provided by the collaborating institutions from
 99 USA, Italy, UK, and Canada. The apparatus and DAQ installation will start in 2020 and
 100 the data taking run is expected to be in summer-fall 2021.

101 The neutron form factors are challenging to be determine experimentally especially be-
 102 cause there is no free neutron target. However, since the deuterium is a loosely coupled
 103 system, it can be viewed as the sum of a proton target and a neutron target. In fact, quasi-
 104 elastic scattering from deuterium has been used to extract the neutron magnetic form factor,
 105 G_M^n , at modestly high Q^2 for decades [20, 21] in the single arm (e, e') experiments. How-
 106 ever, the proton cross section needs to be subtracted by applying a single-arm quasi-elastic
 107 electron-proton scattering. This “proton-subtraction” technique suffers from a number sys-
 108 tematic uncertainties e.g. contributions from inelastic and secondary scattering processes.

109 Many year ago, L. Durand [22] proposed the so-called “ratio-method” based on the mea-
 110 surement of both $D(e, e'n)$ and $D(e, e'p)$ reactions. In this method, many of the systematic
 111 errors are cancel out. Several experiments [23–25] have applied the ratio-method to deter-
 112 mine the neutron magnetic form factor.

113 The GMn/SBS experiment [19] will take data for elastic $e - n$ scattering for several
 114 kinematics with Q^2 from 3.5 up to 13.5 $(\text{GeV}/c)^2$. We propose to use this method to
 115 measure Rosenbluth slope and extract (in OPE approximation) the neutron electric form
 116 factor, G_E^n , at one value of momentum transfer. In fact, one of required data points will
 117 be taken by the GMn experiment, so an additional measurement is needed only for one
 118 kinematics.

119 Data will be collected for quasi-elastic electron scattering from deuteron in process
 120 $D(e, e'n)p$. A complementary $D(e, e'p)n$ data will be taken to calibrate the experiment ap-
 121 paratus. The current knowledge of the $e - p$ elastic scattering cross section (obtained in the
 122 single arm $H(e, e')p$ and $H(e, p)e'$ experiments) will be also used for precision determination

¹²³ the experiment kinematics.

¹²⁴ Applying Rosenbluth technique to measure G_E^n requires accurate measurement of the cross
¹²⁵ section and suffers from large uncertainties. To overcome this issue, we propose to extract
¹²⁶ the value of G_E^n from the ratio of quasi-elastic yields, $R_{n/p}$, in scattering from a deuteron
¹²⁷ target as follows:

$$R_{n/p} \equiv R_{observed} = \frac{N_{e,e'n}}{N_{e,e'p}} \quad (5)$$

¹²⁸ $R_{observed}$ needs to be corrected to extract the ratio of e-n/e-p scattering from nucleons:

$$R_{corrected} = f_{corr} \times R_{observed} , \quad (6)$$

¹²⁹ where the correction factor $f_{correction}$ takes into account the variation in the hadron efficiencies
¹³⁰ due to changes of $e - N$ Jacobian, the radiative corrections, and absorption in path from the
¹³¹ target to the detector, and small re-scattering correction.

¹³² In one-photon approximation, $R_{corrected}$ can be presented as:

$$R_{corrected} = \frac{\sigma_{Mott}^n \cdot (1 + \tau_p)}{\sigma_{Mott}^p \cdot (1 + \tau_n)} \times \frac{\epsilon \sigma_L^n + \sigma_T^n}{\epsilon \sigma_L^p + \sigma_T^p} \quad (7)$$

It is important that the ratio $R_{Mott} = \frac{\sigma_{Mott}^n \cdot (1 + \tau_p)}{\sigma_{Mott}^p \cdot (1 + \tau_n)}$ could be determine with very high relative accuracy even with modest precision for the beam energy, electron scattering angle, and detector solid angle. Now, let us write the $R_{corrected}$ at two values of ϵ using $R_c^{n(p)} = \sigma_L^{n(p)} / \sigma_T^{n(p)}$ as:

$$R_{corrected,\epsilon_1} = R_{Mott,\epsilon_1} \times \frac{\epsilon_1 \sigma_L^n + \sigma_T^n}{\epsilon_1 \sigma_L^p + \sigma_T^p} \quad R_{corrected,\epsilon_2} = R_{Mott,\epsilon_2} \times \frac{\epsilon_2 \sigma_L^n + \sigma_T^n}{\epsilon_2 \sigma_L^p + \sigma_T^p}$$

In these two equations there are two unknown variables: σ_L^n and σ_T^n . The dominant contribution to the uncertainty of the slope of the cross section vs. ϵ , $S_c^n = \sigma_L^n / \sigma_T^n$, will come from the uncertainty of S_c^p . At $Q^2=4.5$ (GeV/c)², according to the global analysis of $e - p$ cross section [3], the value of S_c^p is close to $1/(\tau \mu_p^2) = 0.107$ with uncertainty of 0.01. The resulting equation for S_c^n is:

$$A = B \times \frac{1 + \epsilon_1 S_c^n}{1 + \epsilon_2 S_c^n} \approx B \times (1 + \Delta \epsilon \cdot S_c^n),$$

where the variable $A = R_{corrected,\epsilon_1}/R_{corrected,\epsilon_2}$ will be measured with relative precision of 0.1%. Assuming, for this estimate, equal values of Q^2 for two kinematics, the τ and σ_T for two kinematics are canceled out, and the variable $B = R_{M,\epsilon_1}/R_{M,\epsilon_2} \times (1 + \epsilon_2 S_c^p)/(1 + \epsilon_1 S_c^p)$. For actual small range of ϵ and small value of the slope, the $B \approx (1 - \Delta\epsilon \cdot S_c^p)$. The value of B will be determined from global proton $e - p$ data to a precision of 0.25×0.01 .

At $Q^2=4.5$ (GeV/c) 2 the ratio $\mu_n G_E^n/G_M^n$ is of 0.55 ± 0.05 , see the review [26]. In a simplest model, the slope S_c^n is a sum of the slope due to G_E^n/G_M^n and the TPE contribution. If we use for TPE the prediction [4], shown in Fig. 2, the TPE leads to increase of S_c^n by a factor of 2, so the result of this experiment for TPE will be $0.069 \pm 0.012 \pm 0.01$, where the first uncertainty is due to accuracy of G_E^n/G_M^n and the second one due to projected precision of this experiment. It would be a 4-4.5 sigma observation of the neutron TPE.

144

IV. PROPOSED MEASUREMENTS

145 We propose to use the same experimental setup of E12-09-019 experiment. We will add
 146 a kinematic point at $Q^2 = 4.5 \text{ (GeV/c)}^2$, but with a higher ϵ value. This additional point
 147 along with the data point of E12-09-019 experiment will allow us to perform the standard
 148 Rosenbluth method to obtain (in one-photon approximation) the neutron electric and mag-
 149 netic form factors. In addition, the "Super-Rosenbluth" technique, in which the systematic
 150 errors are greatly reduced, will be implemented to calculate the two photon exchange (TPE)
 151 contribution. The study of the ϵ dependance two photon exchange contribution to the neu-
 152 tron form factor ratio G_E^n/G_M^n . Table. I displays the kinematic settings of the proposed
 153 experiment.

Point	Q^2 (GeV/c) ²	E (GeV)	E' (GeV)	θ_{BB} degrees	θ_{SBS} degrees	ϵ
1	4.5	4.4	2.0	41.88	24.67	0.599
2	4.5	6.6	4.2	23.23	31.2	0.838

TABLE I. Kinematic settings of the proposed experiment. The kinematic point with the lowest ϵ value (blue raw) is an existing measurement of the approved E12-09-019.

154

V. EXPERIMENTAL SETUP

155 As illustrated in Fig. 3, this experiment will study electron scattering from a 15 cm
 156 long liquid Deuterium target held in a vacuum. The scattered electron will be detected
 157 in the BigBite spectrometer with an upgraded electron detector stack. The neutron arm is
 158 arranged with a dipole magnet 48D48 (SBS) and a segmented hadron calorimeter HCAL. The
 159 whole detector package was designed and is now under assembling for the GMn, E12-09-019,
 160 experiment.

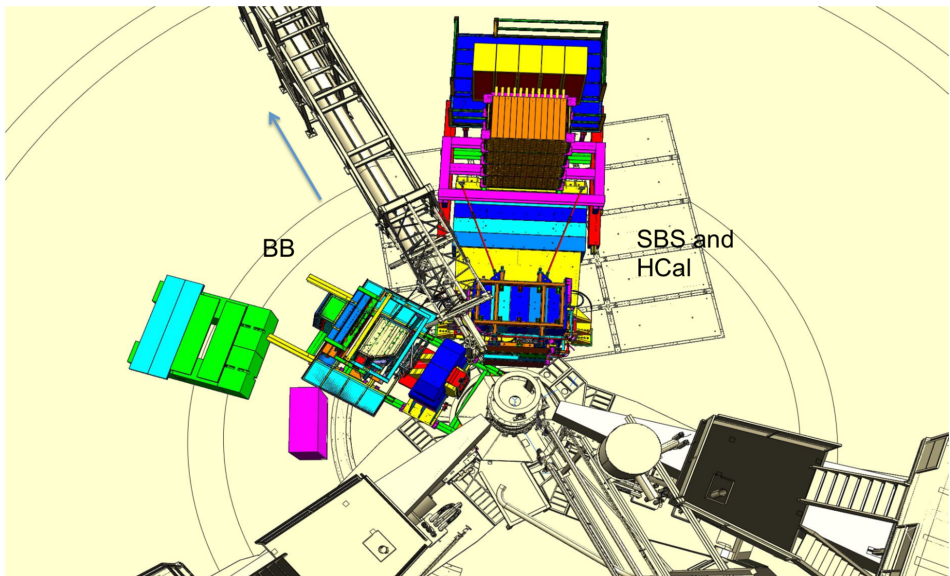


FIG. 3. Layout of the experimental setup in nTPE.

161

1. Parameters of the SBS

162 The 48D48 magnet from Brookhaven was acquired as part of the Super Bigbite project
 163 and will be available for this experiment. It consists of a large dipole magnet which provides
 164 a field integral of about $1.7 \text{ T} \cdot \text{m}$, allowing for quasielastic protons to be sufficiently deflected
 165 to allow clear differentiation from neutrons. The active field volume has an opening of $46 \times$
 166 $25 \text{ vertical} \times \text{horizontal}$), matching the aspect ratio of the neutron arm, and a depth of 48
 167 cm.

¹⁶⁸ The placement of this magnet will be 1.6 m away from the target, which would normally
¹⁶⁹ interfere with the beamline. To accommodate this, modifications were made to the iron yoke
¹⁷⁰ such that the beamline will pass through the magnet yoke area.

¹⁷¹ The field configuration will be such that positively charged particles will be deflected
¹⁷² upwards away from the hall floor. For a field integral of 1.7 Tesla-m, protons of momentum
¹⁷³ 2.5 GeV/c will be deflected 250 mrad, which translates to a displacement of xxm. Including
¹⁷⁴ expected detector resolution, the $p_{miss,\perp}$ distribution will be similar to what was seen in
¹⁷⁵ E02-013, so cuts of < 100 MeV/c will be appropriate. Monte Carlo simulations show a
¹⁷⁶ contamination of charged quasielastics to be negligible.

¹⁷⁷ The presence of the magnet also works to sweep low energy charged particles from the
¹⁷⁸ target away from the neutron arm. Particles of momentum less than 1.3 GeV/c will be
¹⁷⁹ entirely swept outside of the neutron arm acceptance. This greatly reduces the amount of
¹⁸⁰ charged low energy background.

181

A. The BigBite Spectrometer

182 Scattered electrons will be detected in the BigBite spectrometer. The spectrometer con-
 183 sists of a single dipole magnet (with magnetic field approximately 1.2 T) and a detection
 184 system, see Fig. 4.

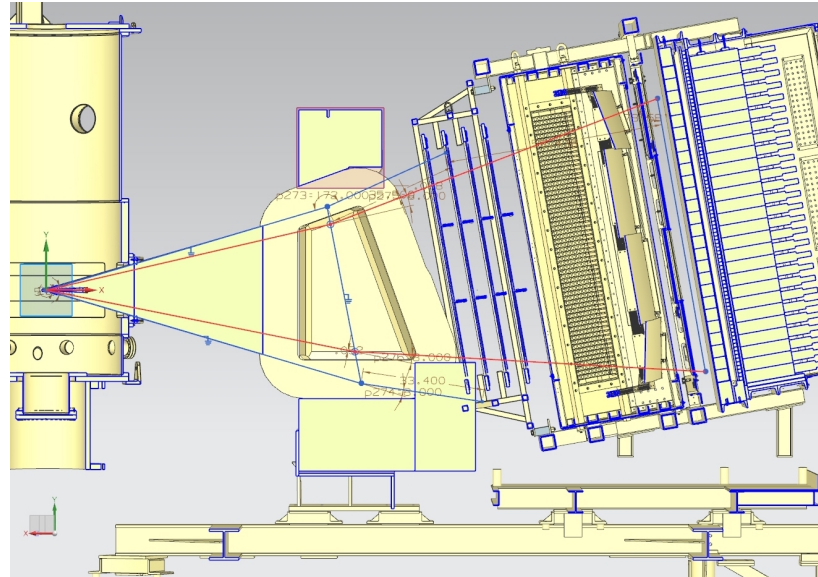


FIG. 4. The BigBite spectrometer with the upgraded detector stack.

185

1. GEM Chambers

186 To perform the tracking of charged particles under the high rates anticipated for this
 187 experiment, the drift chambers were replaced with gas electron multiplier (GEM) detectors.
 188 These detectors have proven to be capable of operating under luminosities of 25 kHz/mm^2
 189 for the COMPASS experiment at CERN and the spatial resolution of each of these chambers
 190 is anticipated to be about $70 \mu\text{m}$. There will be two sets of GEMs placed on each side of the
 191 GRINCH Cherenkov detector.

192 The set of GEMs in front of the GRINCH is composed of four layers of GEMs. Two of
 193 these layers have been built by will the SBS collaborators from INFN. They are composed

¹⁹⁴ three modules each, measuring $40 \times 50 \text{ cm}^2$, such that each layer covers $40 \times 150 \text{ cm}^2$ (the
¹⁹⁵ long dimension being vertical, along the dispersive direction). The readout of these modules
¹⁹⁶ are oriented in the x/y direction *i.e.* parallel and perpendicular to the dispersive direction
¹⁹⁷ (horizontal and vertical). The two other layers are being built by the SBS collaborators from
¹⁹⁸ UVA. They are composed of a single module measuring $40 \times 150 \text{ cm}^2$, the long dimension
¹⁹⁹ again being vertical and along the dispersive direction. The readout of these modules are
²⁰⁰ oriented in the u/v direction *i.e.* ± 30 degrees with respect to the horizontal direction.

²⁰¹ The set of GEMs behind the GRINCH has been built by the SBS collaborators from
²⁰² UVA. It is composed of a single layer composed of four modules measuring $50 \times 60 \text{ cm}^2$,
²⁰³ such that the layer covers $60 \times 200 \text{ cm}^2$ (the long dimension again being along the dispersive
²⁰⁴ direction). The readout of these modules are all oriented in the x/y direction.

²⁰⁵ The level background in the GEMs have been evaluated, thanks to G4SBS ([27] abd
²⁰⁶ Sec. VI) for the G_M^n experimental readiness review. For the G_M^n highest Q^2 point (which is the
²⁰⁷ most constraining, since it combines mandatory maximum luminosity and smaller BigBite
²⁰⁸ angles, the background level in the front GEMs are of the order of 120 kHz/cm^2 for the front
²⁰⁹ GEM layers, and below 50 kHz/cm^2 for the back GEM. To perform the GEM tracking within
²¹⁰ such a background environment, we use the cluster reconstructed in the BigBite shower as
²¹¹ a track seed to clean the large combinatorics that would otherwise be created by the large
²¹² number of hits. After this, the main challenge is the separation by the clustering algorithm
²¹³ of the signal and background hits to minimize track smearing. At this level of background, a
²¹⁴ TreeSearch tracking algorithm combined with a fairly simple cluster separation algorithm has
²¹⁵ already proven to achieve 70% efficiency at nominal luminosity. A better cluster separation
²¹⁶ algorithm is currently being developed and should allow to significantly improve this figure.

²¹⁷ 2. Shower/Preshower

²¹⁸ The electromagnetic calorimeter configuration consists of two planes of lead glass blocks
²¹⁹ which we call the preshower and shower. The preshower, located about 80 cm behind
²²⁰ the first GEM chamber, consists of a 2×26 plane of $37 \text{ cm} \times 9 \text{ cm}$ blocks. The shower, about
²²¹ 1 m behind the first GEM chamber, consists of an 7×27 array of $8.5 \text{ cm} \times 8.5 \text{ cm}$ blocks.

²²² Sums over these blocks form the physics event trigger for the experiment.

²²³ The preshower signal can be used to provide an additional method of pion rejection.

²²⁴ By selecting low preshower signals, a pion rejection factor of 1:50 can be achieved through
²²⁵ optimization. Despite higher particle rates, pion rejection performance is anticipated to
²²⁶ be similar to that achieved for Transversity, E06-010. By measuring the pedestal widths
²²⁷ and resolution for E06-010 and scaling to this proposal's conditions, overall relative energy
²²⁸ resolution for the detector is expected to become worse by a factor of 1.6, to about $\sigma_{\delta E/E} =$
²²⁹ 25%.

²³⁰ 3. Timing hodoscope

²³¹ The BigBite timing hodoscope has been built the the SBS collaborators from Glasgow,
²³² to replace the BigBite scintillator plane. It will be composed of 90 bars stacked in a plane,
²³³ each with dimensions 1 in. \times 1 in. \times 60 cm. The paddle stack will be oriented such as
²³⁴ the long dimension of the bars is horizontal *i.e.* perpendicular to the dispersive direction.
²³⁵ Each of these elements are readout by a PMT on each side, mostly to provide measurement
²³⁶ redundancy.

²³⁷ This plane will primarily be used to provide a signal for nucleon time of flight reconstruc-
²³⁸ tion. A time resolution of 200 ps is anticipated. This fine segmentation is meant to lower the
²³⁹ rates in the detector. Background studies made for the G_M^n experimental readiness review
²⁴⁰ demonstrated that the rates experienced by each element was \leq 500 kHz at a luminosity of
²⁴¹ 2.8×10^{38} cm $^{-2}$ s $^{-2}$. The PMTs pulses are processed by NINO front-end cards which, when
²⁴² the PMT pulse crosses the NINO threshold, will produce a digital signal to be readout by
²⁴³ CAEN 1190 TDCs which record a leading time and a trailing time.

²⁴⁴ 4. GRINCH cherenkov detector

²⁴⁵ The main purpose of the Ring Imaging Cherenkov is to provide additional particle iden-
²⁴⁶ tification for offline pion rejection. The GRINCH consists of a tank with a maximum depth
²⁴⁷ of 88.9 cm, with 4 cylindrical mirrors focussing the cherenkov light directly onto a 510 PMT

²⁴⁸ array (60 lines of PMTs, with lines of 9 PMTs alternating with lines of 8 PMTs) placed away
²⁴⁹ from the beam. The radiation gas will be C_4F_8 , which is by far the best compromise between
²⁵⁰ light yield for electrons and operating cost. With $n - 1 = 1.35 \times 10^{-3}$, the π threshold is only
²⁵¹ about 2.7 GeV, so the additional pion rejection will be most effective below this threshold.

²⁵² As for the timing hodoscope The PMTs pulses are processed by NINO front-end cards
²⁵³ which, when the PMT pulse crosses the NINO threshold, will produce a digital signal to
²⁵⁴ be readout by VETROC TDCs, which for each PMT hit will record a leading time and a
²⁵⁵ trailing time. The analog signal will not be recorded however, which means that for each
²⁵⁶ PMT hit, the information of the number of not directly available (although it can in theory
²⁵⁷ be deduced from the time over threshold).

²⁵⁸ All of this implies that the electron selection relies on the number of GRINCH PMT
²⁵⁹ firing, instead of relying on the signal amplitude.

260

B. Hadron Calorimeter (HCal)

261 The Hadron Calorimeter (HCal) has been designed specifically to measure the recoil
 262 nucleon for the SBS experiments. Specifically for this experiment (and for G_M^n), HCal
 263 combined with the SBS (48D48) magnet provides identification of the recoil nucleon, as
 264 well as additional kinematic constraint and possibly timing information on the measured
 265 interaction. Nucleon identification is illustrated on Fig. 5. This figure shows the compared
 266 proton and neutron position distribution in HCal at the same electron kinematics. The
 267 proton distribution is being shifted upwards by about 1 m compared to the neutron.

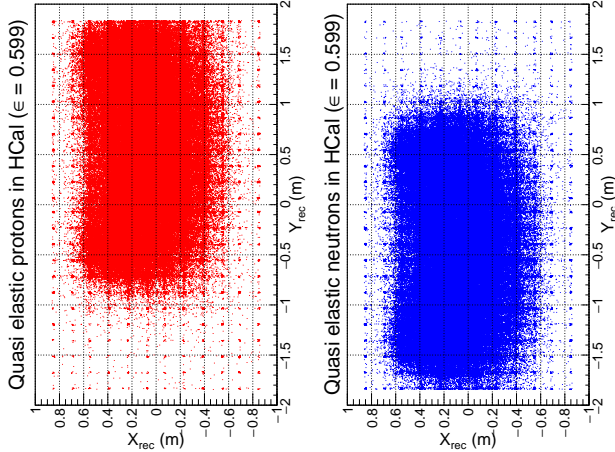


FIG. 5. Reconstructed HCal cluster from quasi-elastic events generated by G4SBS. The left distribution in red is for the proton, the right distribution in blue is for the neutron.

268
269

270 The HCal (which CAD model is shown on Fig. 6) is composed of 288 modules arranged in
 271 an array of 12×24 . In front of the full assembly is located a $3/4$ in steel plate which purpose
 272 is double:

- 274 • initiate the hadronic shower to optimize the calorimeter response;
 - 275 • shield the modules from a fraction of the low energy secondaries;
- 276 Each of these modules measures $6 \times 6 \text{ in}^2$ section, for 3 ft length. They are composed of
 277 alternating tiles of scintillators and iron around a central light guide which collects the light

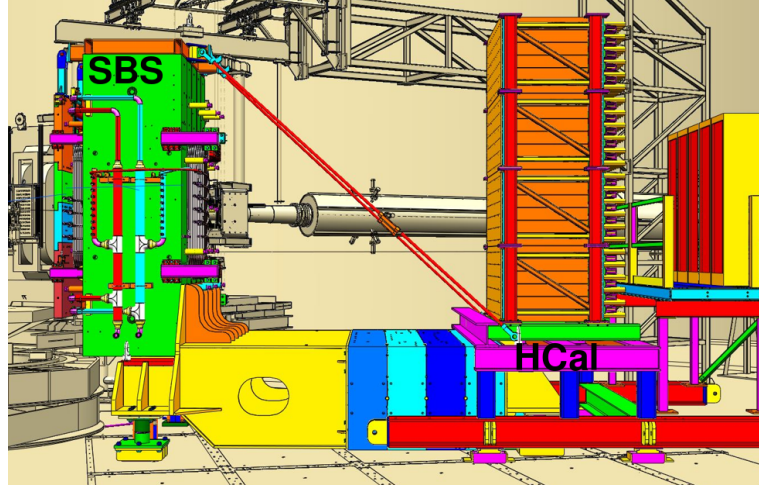


FIG. 6. CAD representation of HCal (right) with the SBS magnet (left)

²⁷⁸ generated in the scintillators by the hadronic shower, and guides it to the PMT at the end of
²⁷⁹ the block. Cosmics tests have determined that the average light yield for the HCal modules
²⁸⁰ is around 5 photoelectrons per MeV deposited in the scintillator tiles.

²⁸¹ The PMTs are readout with FADC250 which sample the PMT signal every 4 ns and allow
²⁸² to reconstruct the PMT pulse shape, hence its timing. They are also readout by TDCs which
²⁸³ provide additional timing information. Thanks to this, the timing resolution can be better
²⁸⁴ than 1 ns, which cosmics tests (in progress) seem to confirm.

²⁸⁵ The energy resolution is intrinsically broad (see Fig. 9 in Section VI), due mostly to the
²⁸⁶ small fraction of energy from the hadronic shower actually measured by the scintillator tiles
²⁸⁷ (≤ 0.1 - refer yet again to Fig. 9).

288 **VI. SIMULATIONS, ESTIMATIONS OF COUNTING RATES AND**
 289 **ACCIDENTALS**

290 The estimations of counting rates accidentals have been performed using G4SBS, the
 291 GEANT4-based simulation package developed for the SBS experiment [27]. This package
 292 includes a wide range of event generators, which allows to evaluate the rates for both events
 293 of interest (signal) and background. The representation of the experiment apparatus in
 294 G4SBS is shown in the high ϵ configuration on Fig. 7.

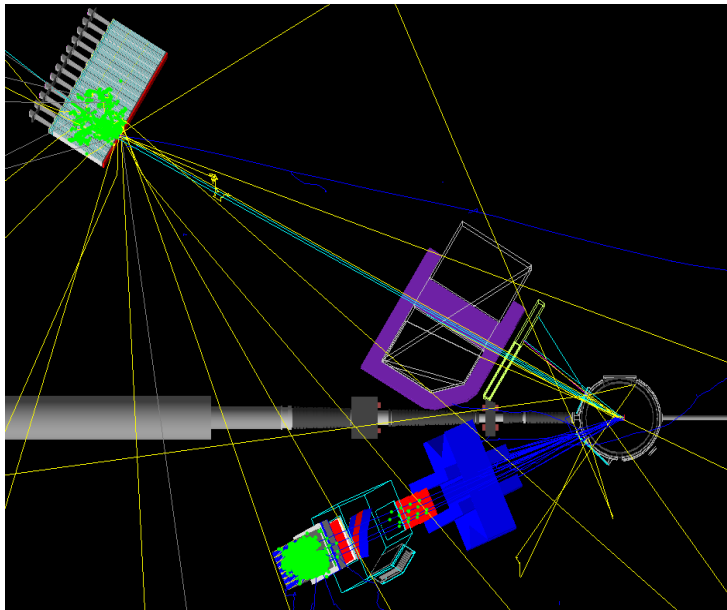


FIG. 7. Top view of the experimental apparatus model in G4SBS, shown in the high ϵ configuration. The beam direction is indicated, as well as the main elements (HCal, SBS magnet, BigBite spectrometer)

295 **A. Background and trigger rates**

296 The main processes expected to contribute the trigger rates for the BigBite spectrometer
 297 are:

- 298 • the inelastic electron nucleon scattering process;

- 299 • photons from inclusive π^0 production;

- 300 • and to a lesser extent, charged pions.

301 One the other hand, we expect all sorts of hadronic backgrounds to contribute to the rates in
 302 HCal, the dominant ones being pions. Both the inelastic scattering and the inclusive neutral
 303 and charged pion production are implemented in G4SBS, the latter relying on the Wiser
 304 parametrization [28]. We may also considered the minimum-bias “beam-on-target” gener-
 305 ator for the HCal background, especially at lower angle (all electromagnetic and hadronic
 306 processes being built-in in G4SBS).

307 The thresholds to apply to each arm are determined as a function of the elastic peak. For
 308 the electron arm, the threshold has been set at $\mu_E - 2.5\sigma_E$, μ_E and σ_E being respectively
 309 the position and width of the fitted elastic peak. Fig. 8 presents the distributions of rate of
 310 energy deposit for the different processes involved in the BigBite trigger rates.

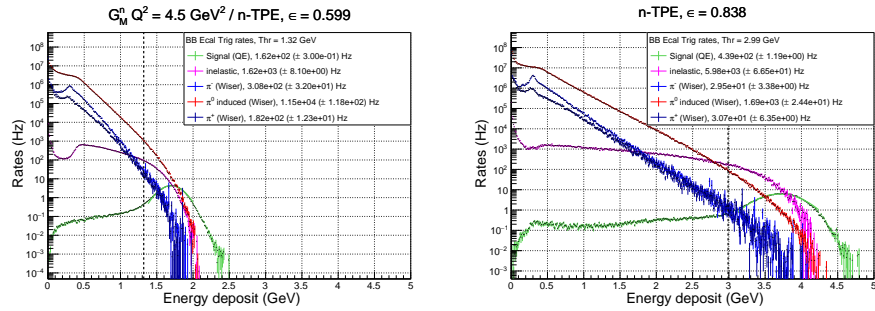


FIG. 8. Rates of the different process contributing to the BigBite electron arm trigger, for the low ϵ (left) and the high ϵ (right). Quasi-elastic is in green, inelastic in magenta, π^0 in red, π^- in blue, and π^+ in dark blue. Note the resolution for the elastic peak in the BigBite shower is ~ 0.3 GeV.

311 Since HCal is a sampling calorimeter (meaning that only a fraction of the shower energy
 312 is measured), it's resolution is significantly wider (~ 0.7 GeV). Due to this, the threshold
 313 is at 90% efficiency (which corresponds to ~ 0.1 GeV for both kinematics. Fig. 9 presents
 314 the distributions of rate of energy deposit for the different processes involved in the BigBite
 315 trigger rates.

317 The thresholds and trigger rates for each arm, as well as the coincidence rate (assuming

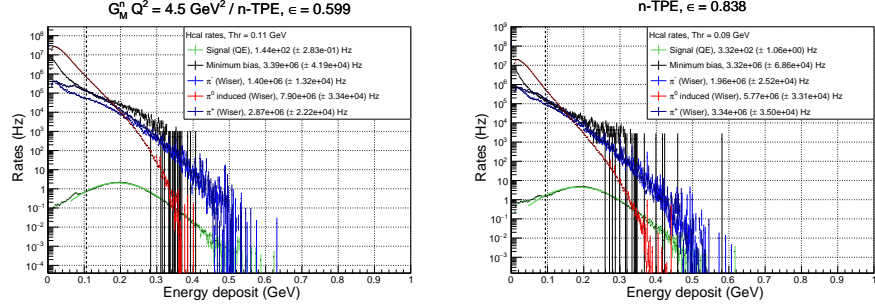


FIG. 9. Rates of the different process contributing to the HCal trigger, for the low ϵ (left) and the high ϵ (right). Quasi-elastic is in green, minimum bias in black, π^0 in red, π^- in blue, and π^+ in dark blue. Note the peak itself is around 0.2 GeV for 3.2 GeV nucleons.

319 30ns coincidence window), are summarized in Table. II. Note that for HCal, the “total
320 rates” is either the sum of inclusive charged and neutral pions evaluated with the Wiser
321 cross sections *or* the “minimum bias” beam on target. We have good reasons to think that
322 the Wiser code results actually overestimate the HCal rates, but for the sake of thoroughness,
323 we have checked the coincidence rates assuming the sum of the inclusive pions (evaluated
324 with the Wiser cross sections) as the HCal rates.

325 In the worst case scenario, the coincidence rates could be as high as 5kHz, which might be
326 at the limit of manageability for the DAQ. However, a slight increase on the HCal threshold
327 (which would drop the efficiency from ~90% to ~85%) would decrease the total HCal rates by
328 ~35% to 40% in this worst case scenario, which would make the situation more manageable
329 (3.3 kHz).

330

B. Contamination from inelastic

331 The main source of contamination for the quasi-elastic comes from the inelastic electron-
332 nucleon scattering. Most of this contamination can be cleaned out thanks to a selection on
333 the center of mass energy

$$W^2 = M_N^2 + 2M_N^2(E - E') - Q^2, \quad (8)$$

Point (ϵ)	1 (0.599)		2 (0.838)	
	BigBite rates (Hz)	HCal rates (Hz)	BigBite rates (Hz)	HCal rates (Hz)
threshold (GeV)	1.32	0.106	2.99	0.090
Quasi-elastic	1.62×10^2	1.44×10^2	4.39×10^2	3.48×10^2
Inelastic	1.62×10^3	-	5.98×10^3	-
π^- (Wiser)	3.08×10^2	1.40×10^6	2.95×10^2	1.96×10^6
π^0 (Wiser)	1.15×10^4	7.90×10^6	1.69×10^3	5.77×10^6
π^+ (Wiser)	1.82×10^2	2.87×10^6	3.07×10^2	3.34×10^6
Minimum bias	-	3.39×10^6	-	3.32×10^6 (*)
<i>Total</i>	1.37×10^4	1.22×10^7	8.17×10^3	1.11×10^7
(min. bias - HCal only)		/ 3.39×10^6		/ 3.32×10^6
Coincidence rate	5.01×10^3		2.72×10^3	
(with min. bias HCal)	1.39×10^3		8.14×10^2	

TABLE II. Trigger rates for BigBite and HCal, with the different process contributions separated, and the sum. For HCal, the total rates is either the sum of the (Wiser) inclusive pions or the minimum bias. The coincidence rates assume a 30 ns coincidence window.

and the missing transverse momentum of the nucleon

$$p_{\perp miss} = \sqrt{(q_x - p'_x)^2 + (q_y - p'_y)^2}, \quad (9)$$

where M_N is the mass of the nucleon, E and E' the initial and final energy of the electron, and $q_{x,y}$, $p'_{x,y}$ are the projections on x , y of the vectors of the virtual photon and final nucleon. The distributions of these quantities (weighted with cross section and including detector resolutions) are displayed for quasi-elastic and inelastic scattering, and for proton and nucleon, on Fig. 10 for the low ϵ kinematic, and on Fig. 11 for the high ϵ kinematic.

Provided that we are not limited by statistics and the sample purity is capital for our experiment, we set the selection criteria on W^2 and $p_{\perp miss}$ to maximize inelastic contamination (ideally below 1 %). Setting $p_{\perp miss} \leq 0.1$ GeV and $W^2 \leq 1.1$ GeV 2 , the inelastic

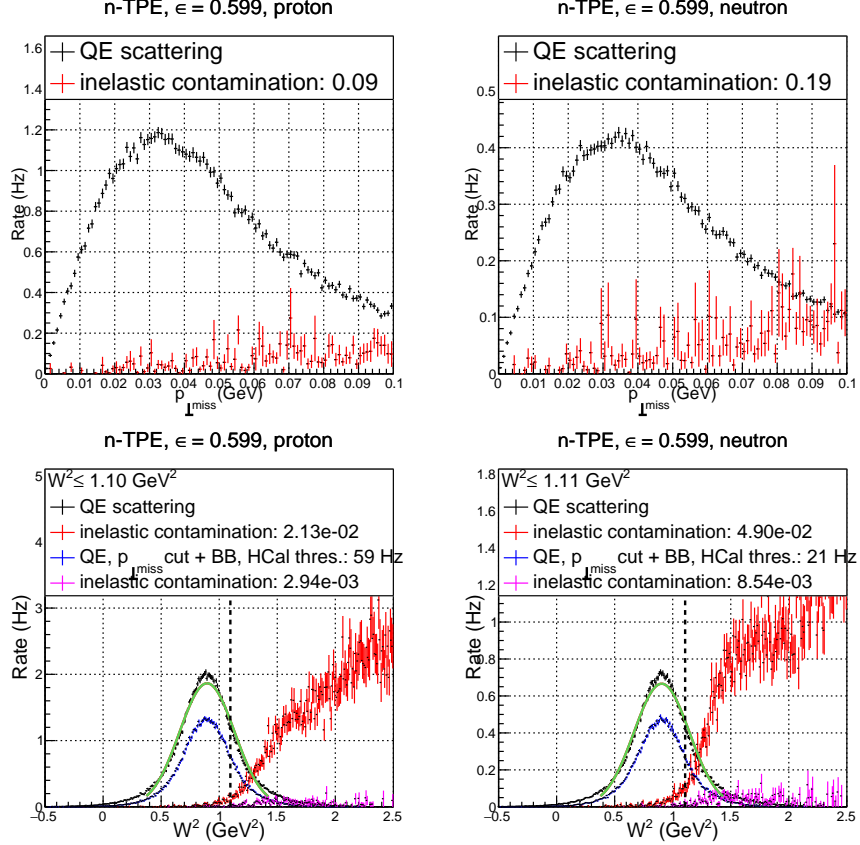


FIG. 10. Compared quasi-elastic and inelastic distributions (including detectors resolutions) for $p_{\perp\text{miss}}$ (top) and W^2 (bottom), for the low ϵ kinematic. Comparison for protons is on the left, and comparison for neutrons is on the right. On the bottom panel, black and red are before the $p_{\perp\text{miss}} \leq 0.1$ GeV selection, while blue and magenta are after $p_{\perp\text{miss}} \leq 0.1$ GeV selection and application of BigBite shower and HCal thresholds.

³⁴³ contamination of the elastic sample ranges from 0.2 % to 0.9 %, while retaining ≥ 60 % of
³⁴⁴ the quasi-elastic events properly recorded in the BigBite-SBS pair. Table. III summarizes
³⁴⁵ the quasi-elastic selection cuts, ad inelastic contamination δ_{inel} .

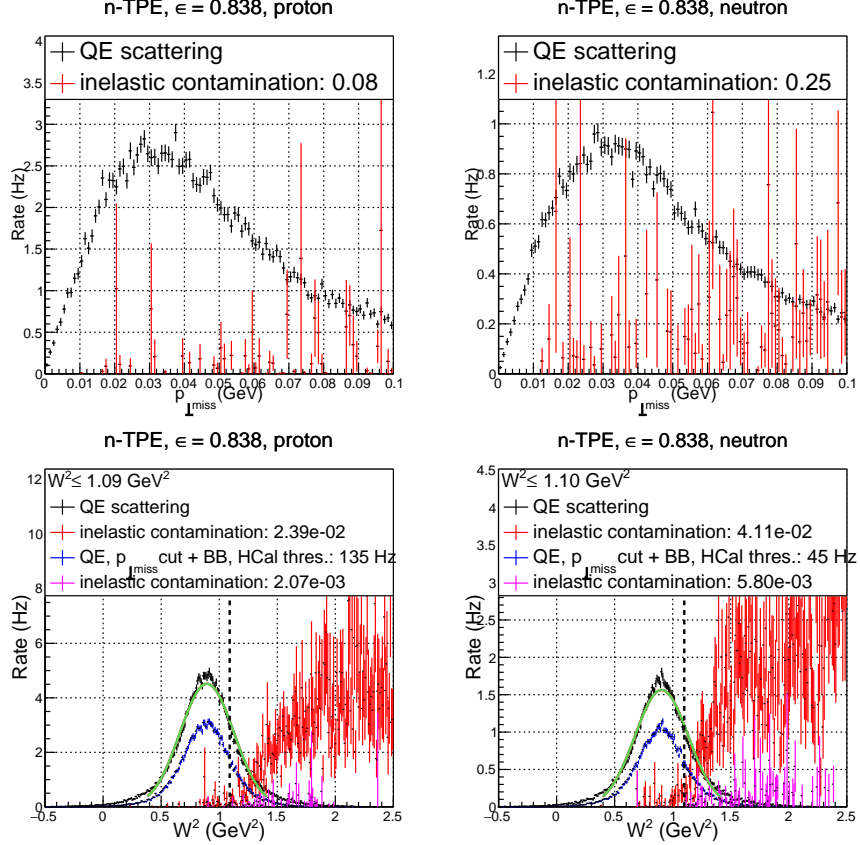


FIG. 11. Compared quasi-elastic and inelastic distributions (including detectors resolutions) for $p_{\perp\text{miss}}$ (top) and W^2 (bottom), for the high ϵ kinematic. Comparison for protons is on the left, and comparison for neutrons is on the right. On the bottom panel, black and red are before the $p_{\perp\text{miss}} \leq 0.1$ GeV selection, while blue and magenta are after $p_{\perp\text{miss}} \leq 0.1$ GeV selection and application of BigBite shower and HCal thresholds.

346

C. Quasi-elastic counting rates

347 The signals for this experiment have been generated using the G4SBS elastic/quasi-elastic
 348 generator. We generated a reasonably large sample of quasi-elastic events N_{Gen} for each
 349 kinematics, on a solid angle $\Delta\Omega_{\text{Gen}}$ that was larger than the detector acceptance. To evaluate
 350 the detector solid angle, we define simple criteria that each event has to pass, defined as the
 351 following;

Point (ϵ)	N	W^2 cut	$p_{\perp miss}$ cut	δ_{inel}
1 (0.599)	n	1.10	0.10	2.94×10^{-3}
	p	1.11	0.10	8.54×10^{-3}
2 (0.838)	n	1.09	0.10	2.07×10^{-3}
	p	1.10	0.10	5.80×10^{-3}

TABLE III. Summary of cuts for quasi-elastic selection and resulting inelastic contamination δ_{inel} .

- 352 • require a primary track, going through all 5 GEM layers (electron arm);
 353 • require non-zero energy deposit in both the preshower and shower (electron arm);
 354 • require non-zero energy deposit in HCal (hadron arm).

355 The detector solid angle, for both proton and neutron, are defined in Table. IV. We also
 356 define there the p - n acceptance asymmetry $A_{\Delta\Omega}$ such as:

$$A_{\Delta\Omega} = \frac{(\Delta\Omega_e \otimes \Delta\Omega_n) - (\Delta\Omega_e \otimes \Delta\Omega_p)}{(\Delta\Omega_e \otimes \Delta\Omega_n) + (\Delta\Omega_e \otimes \Delta\Omega_p)} \quad (10)$$

Point (ϵ)	$\Delta\Omega_e$ (msr)	$\Delta\Omega_e \otimes \Delta\Omega_n$ (msr)	$\Delta\Omega_e \otimes \Delta\Omega_p$ (msr)	$A_{\Delta\Omega}$ (%)
1 (0.599)	52.4	46.7	47.2	0.5
2 (0.838)	32.7	20.8	22.2	3.0

TABLE IV. Kinematics electron solid angle, and convoluted electron/hadron solid angle, and acceptance asymmetry.

357 Then, we evaluate the detection efficiency. For the electron, we require the energy recon-
 358 structed in the BigBite calorimeter to be above a threshold defined as $thr = \mu_E - 2.5 * \sigma_E$,
 359 as well as a minimum number of GRINCH PMTs fired due to the primary electron; For
 360 HCal, we require the threshold to be such as we obtain 90% efficiency. These values are
 361 summarized in Table. V. Quasi-elastic selection efficiency η_{sel} are also reminded.

362 The counting rates are evaluated using among the N_{Gen} events generated the events that
 363 have passed the selection described below, and weighting those events with the cross section

Point (ϵ)	BB thr. (GeV)	HCal thr. (GeV)	$\eta_{det\ e}$	$\eta_{det\ n}$	$\eta_{det\ p}$	$\eta_{sel\ n}$	$\eta_{sel\ p}$
1 (0.599)	1.32	0.11	0.902	0.904	0.892	0.589	0.605
2 (0.838)	2.99	0.09	0.808	0.889	0.882	0.617	0.647

TABLE V. Kinematics electron thresholds, particle detection efficiencies (η_{det}), and efficiency of quasi-elastic selection η_{sel} separated for the proton and the neutron.

³⁶⁴ $d\sigma/d\Omega|_i$ calculated by G4SBS, multiplied by the generation solid angle $\Delta\Omega_{Gen}$, using the
³⁶⁵ formula:

$$N_{est} = \frac{\mathcal{L}_{exp}\Delta t}{N_{Gen}} \times \sum_{i \in accepted\ evts} \left(\frac{d\sigma}{d\Omega} \Big|_i \times \Delta\Omega_{Gen} \right) , \quad (11)$$

³⁶⁶ where Δt the running time and \mathcal{L}_{exp} the experimental luminosity. \mathcal{L}_{exp} can be calculated as
³⁶⁷ follows:

$$\mathcal{L}_{exp} = \frac{I_{exp}}{q_e} \cdot L_{tgt} \cdot d_{tgt} \frac{N_A}{m_D} , \quad (12)$$

³⁶⁸ where I_{exp} is the beam current, q_e is the electron charge, L_{tgt} and d_{tgt} are the target length
³⁶⁹ and density respectively, N_A is Avogadro's number, and m_D is the deuterium mass number.

³⁷⁰ Events are “accepted” if they meet the following criteria:

- ³⁷¹ • the electron is in the BigBite acceptance;
- ³⁷² • the electron passes the BigBite threshold defined in Table V and gives signal in the
³⁷³ GRINCH;
- ³⁷⁴ • the nucleon is in the HCal acceptance and passes the HCal threshold defined in Table V;
- ³⁷⁵ • the event passes the quasi-elastic selection defined in the previous section *i.e.* $W^2 \leq 1.1 \text{ GeV}^2$
³⁷⁶ and $p_{\perp miss} \leq 0.10 \text{ GeV}$.

³⁷⁷ The total quasi-elastic statistics N_{QE} , as well as the total form factor, F^2 :

$$F^2 = \frac{N_{QE}}{\mathcal{L}_{exp} \cdot \Delta t \cdot d\sigma_{Mott}/d\Omega \cdot \Delta\Omega \cdot \eta} \quad (13)$$

³⁷⁸ and its statistical error $\Delta F^2 = F^2/\sqrt{N_{QE}}$ are compiled for both kinematics in Table. V,
³⁷⁹ assuming a running time $\Delta t = 12$ hours of running at a beam intensity of $I_{exp} = 30 \mu\text{A}$ on

³⁸⁰ a liquid deuterium target with length $l_{tgt} = 15$ cm and density $d_{tgt} = 0.169$ g.cm⁻³. In
³⁸¹ Eq.13, $\Delta\Omega$ is the convoluted BigBite-HCal solid angle, and η is the product of all efficiencies
³⁸² (detection efficiencies η_{det} \times selection efficiency η_{sel}).

Point (ϵ)	N_{QE} (e-n)	N_{QE} (e-p)	F_n^2 ($\times 10^{-3}$)	ΔF_n^2 ($\times 10^{-6}$)	F_p^2 ($\times 10^{-3}$)	ΔF_p^2 ($\times 10^{-6}$)
1 (0.599)	9.07×10^5	2.55×10^6	0.99	1.04	2.73	1.70
2 (0.838)	1.94×10^6	5.83×10^6	0.72	0.52	1.93	0.80

TABLE VI. Quasi-elastic counting rates, and total form factor (defined in Eq. 11).

³⁸³ The calculation of the F_2 term requires the evaluation of the Mott cross section:

$$\sigma_{Mott} \equiv \frac{d\sigma_{Mott}}{d\Omega} = (\hbar c \alpha_{EM})^2 \left(\frac{e}{2E} \right)^2 \left(\frac{\cos\theta_e/2}{\sin^2\theta_e/2} \right)^2 \frac{E'}{E} \quad (14)$$

³⁸⁴ The Mott cross section has been calculated with the weighted average of the electron variables
³⁸⁵ (momentum and polar angle).

Point (ϵ)	$\langle \theta_e \rangle$ (deg)	$\langle k' \rangle$ (GeV)	$\langle Q^2 \rangle$ (GeV ²)	σ_{Mott} (nb sr ⁻¹)
1 (0.599)	41.88	2.0	4.5	6.62
2 (0.838)	23.23	4.2	4.5	44.2

TABLE VII. The Mott cross section weighted average of kinematic variables over the BigBite acceptance.

386

VII. SYSTEMATIC ERRORS

387 In this section we will estimate (or set upper limits on) the contributions to the systematic
 388 uncertainty for this experiment. The sources of systematic uncertainties from the experi-
 389 mental setup (target, acceptance, inelastic contamination) were already estimated for the
 390 SBS G_M^n experiment proposal [19]. Note that some of those systematics (nuclear corrections,
 391 accidentals) cancel in the ratio $R = f_{corr} \times N_{e,e'n}/N_{e,e'p}$. Since the experimental setup has
 392 evolved since then, some of these uncertainties have been reevaluated, namely the acceptance
 393 loss and inelastic contamination.

TABLE VIII. Estimated contributions (in percent) to systematic errors on TPE. Quantities marked with * are taken from the SBS G_M^n experiment proposal [19].

Kinematic (ϵ)	(1) 0.599	(2) 0.838
Nuclear correction*	-	
Accidentals*	-	
Target windows*	0.2 %	
Acceptance losses	0.5 %	3.0 %
Inelastic contamination	0.9 %	0.6 %
Nucleon mis-identification*	0.6 %	
Syst. error on $R = f_{corr} \times N_{e,e'n}/N_{e,e'p}$	1.3 %	3.1 %
$S_c^n = \sigma_L^n/\sigma_T^n$	0.107 ± 0.01 (9.3 %)	
$\mu_n G_E^n/G_M^n$	0.55 ± 0.05 (9.1 %)	
Syst. error on TPE	0.069 ± 0.012 (17.4 %)	

394 Table. VIII lists the estimated contributions to systematic errors on the two-photon-
 395 exchange contribution (TPE). The systematics for S_c^n and $\mu_n G_E^n/G_M^n$ have already been ex-
 396 plied in Sec. III, and are the leading contributions to the total uncertainty.

397 Inelastic contamination has been reevaluated in Sec. VI B. To evaluate the upper limit on

³⁹⁸ our uncertainty, we added quadratically the inelastic contamination evaluated for the proton
³⁹⁹ and the neutron for each kinematics, which is the error we make if we ignore the systematics
⁴⁰⁰ completely. Even in this case, we expect less than 1% systematic errors.

⁴⁰¹ The acceptance loss in SBS (*i.e.* the proportion of non-detected nucleons for each detected
⁴⁰² electron) have been evaluated for both kinematics. They are about 10% for the $\epsilon = 0.60$
⁴⁰³ kinematic (meaning that for every good electron measured, we will not measure the recoil
⁴⁰⁴ nucleon 10% of the times), but they are over 30 % for the $\epsilon = 0.84$ kinematics, which is due to
⁴⁰⁵ a larger spread of the nucleon imprint. The systematic uncertainty on the acceptance loss for
⁴⁰⁶ the ratio $R = f_{corr} \times N_{e,e'n}/N_{e,e'p}$ is maximized by the proton-neutron solid angle asymmetry
⁴⁰⁷ $A_{\Delta\Omega} = \Delta\Omega_n - \Delta\Omega_p/\Delta\Omega_n + \Delta\Omega_p$. This asymmetry is about 0.5% for the $\epsilon = 0.60$ kinematic
⁴⁰⁸ (consistent with the G_M^n proposal), but goes up to 3% for the $\epsilon = 0.84$ kinematics.

409

VIII. BEAM TIME REQUEST

410 **We request 48 hours total time (32 hours of beam-on target)** to measure the
 411 two-photon effect (and G_E^n in one-photon approximation) at $Q^2 = 4.5$ (GeV/c)² through a
 412 measurement of the cross sections of the reaction $D(e,e'N)$ at a large value of the virtual
 413 photon polarization $\epsilon=0.84$. *The measurement at $Q^2 = 4.5$ (GeV/c)², $\epsilon=0.60$ is already*
 414 *scheduled as part of the SBS G_M^n experiment E12-09-019 [19].*

415 We plan to take 12 hours of data at a full luminosity of $2.86 \times 10^{38} \text{ cm}^{-2}\text{s}^{-1}$, which
 416 corresponds to a beam intensity of $I_{exp} = 30 \mu\text{A}$ on a liquid deuterium target with length
 417 $l_{tgt} = 15 \text{ cm}$ and density $d_{tgt} = 0.169 \text{ g.cm}^{-3}$. To have a better handle on our backgrounds,
 418 we also plan to take 12 hours of data at half luminosity (basically by lowering the beam
 419 intensity by a factor 2). In each of these configurations, we also need to take data on a
 420 “dummy” target (*i.e.* on a target cell identical to the one used for production, but empty)
 421 to understand the contamination of our data from the target walls.

422 In addition to this beam time, we also require 16 hours (two shifts) to change the exper-
 423 imental configuration. This configuration change means:

- 424 • SBS magnet and the hadronic calorimeter (HCal) angle change;
- 425 • BigBite spectrometer angle and distance change;
- 426 • Beam energy change;

427 These tasks may be done in parallel, but the SBS configuration is the most-time consuming
 428 task, and determines the time required to perform this configuration change. The projected
 429 use of this time is summarized in Table. IX.

430 This experiment will take place in Hall A, along the already scheduled SBS G_M^n experiment
 431 E12-09-019, utilizing the BigBite spectrometer to detect electrons scattered off the liquid
 432 deuterium target, and HCal calorimeter to detect the recoiling neutron and proton.

433 Data taking (if approved by PAC48) will take place in summer 2021 during the approved
 434 and scheduled run of the GMn, E12-09-019, experiment, which is going to measure the $e - n$
 435 elastic scattering cross section at $Q^2 = 4.5$ (GeV/c)² at $\epsilon=0.60$.

Task	Target	I_{exp}	time requested
Data taking (Prod.)	15 cm LD ₂	30 μ A	12 hours
Data taking (Syst.)	15 cm “Dummy”	30 μ A	4 hours
Data taking (Prod.)	15 cm LD ₂	15 μ A	12 hours
Data taking (Syst.)	15 cm “Dummy”	15 μ A	4 hours
Setting changes (SBS, BigBite angles, beam energy)			16 hours
Total			48 hours

TABLE IX. Summary table for the beam time request. Setting changes include SBS and Bigte bite angles change, as well as a beam energy change.

436 The set of instrumentation and required beam current for proposed measurement is iden-
 437 tical to one in the GMn experiment. The beam energy of 6.6 GeV will be used. One of two
 438 data points required for the cross section LT separation is already in the data taking plan of
 439 GMn.

440 There are no other measurements of TPE in the $e - n$ elastic scattering and knowledge
 441 of the TPE is essential for the understanding of the elastic electron scattering from neutron
 442 (and proton) and hadron structure. Furthermore, it is a necessary input in the analysis and
 443 interpretation of a wide range of electron scattering processes.

444 The kinematics of our measurements emphasize the same Q^2 range where TPE in $e - p$
 445 elastic scattering was observed to dominate in Rosenbluth slope. Measuring at this high
 446 momentum transfers will provide unique input for testing TPE calculations [4].

447 We propose to measure the Rosenbluth slope and extract (in one-photon approximation)
 448 $\delta G_E^n/G_M^n$ to an accuracy of 0.15, which would bring its precision to a level comparable with
 449 that of the double polarization experiments GEN-RP and GEN-He3 at such value of Q^2 .
 450 Such precision should be sufficient to detect the TPE contribution to the $e - n$ Rosenbluth
 451 slope on the three sigma level.

-
- 452 [1] R. Hofstadter, *Rev. Mod. Phys.* **28**, 214 (1956).
- 453 [2] M. N. Rosenbluth, *Phys. Rev.* **79**, 615 (1950).
- 454 [3] E. Christy *et al.*, “Two-photon exchange in electron-proton elastic scattering at large four-
455 momentum transfer,” (2020), in preparation for publication in PRL.
- 456 [4] P. G. Blunden, W. Melnitchouk, and J. A. Tjon, *Phys. Rev.* **C72**, 034612 (2005), arXiv:nucl-
457 th/0506039 [nucl-th].
- 458 [5] J. Arrington, P. G. Blunden, and W. Melnitchouk, *Prog. Part. Nucl. Phys.* **66**, 782 (2011),
459 arXiv:1105.0951 [nucl-th].
- 460 [6] A. Afanasev, P. Blunden, D. Hasell, and B. Raue, *Prog. Part. Nucl. Phys.* **95**, 245 (2017),
461 arXiv:1703.03874 [nucl-ex].
- 462 [7] B. Wojtsekhowski, in *Exclusive processes at high momentum transfer. Proceedings, Newport
463 News, USA, May 15-18, 2002* (2002) arXiv:1706.02747 [physics.ins-det].
- 464 [8] G. D. Cates, C. W. de Jager, S. Riordan, and B. Wojtsekhowski, *Phys. Rev. Lett.* **106**, 252003
465 (2011), arXiv:1103.1808 [nucl-ex].
- 466 [9] C. D. Roberts, M. S. Bhagwat, A. Holl, and S. V. Wright, *Eur. Phys. J. ST* **140**, 53 (2007),
467 arXiv:0802.0217 [nucl-th].
- 468 [10] J. Segovia, I. C. Cloet, C. D. Roberts, and S. M. Schmidt, *Few Body Syst.* **55**, 1185 (2014),
469 arXiv:1408.2919 [nucl-th].
- 470 [11] B. Wojtsekhowski (2020) arXiv:2001.02190 [nucl-ex].
- 471 [12] G. A. Miller, *Phys. Rev. Lett.* **99**, 112001 (2007), arXiv:0705.2409 [nucl-th].
- 472 [13] C. E. Carlson and M. Vanderhaeghen, *Phys. Rev. Lett.* **100**, 032004 (2008), arXiv:0710.0835
473 [hep-ph].
- 474 [14] D. Muller, D. Robaschik, B. Geyer, F. M. Dittes, and J. Horejsi, *Fortsch. Phys.* **42**, 101
475 (1994), arXiv:hep-ph/9812448 [hep-ph].
- 476 [15] X.-D. Ji, *Phys. Rev. Lett.* **78**, 610 (1997), arXiv:hep-ph/9603249 [hep-ph].
- 477 [16] A. V. Radyushkin, *Phys. Lett.* **B380**, 417 (1996), arXiv:hep-ph/9604317 [hep-ph].

- ⁴⁷⁸ [17] M. Diehl and P. Kroll, *Eur. Phys. J.* **C73**, 2397 (2013), arXiv:1302.4604 [hep-ph].
- ⁴⁷⁹ [18] N. Kivel, “private communications,” (2020).
- ⁴⁸⁰ [19] J. Annand, R. Gilman, B. Quinn, B. Wojtsekhowski, *et al.*, unpublished. See https://www.jlab.org/exp_prog/proposals/09/PR12-09-019.pdf, https://www.jlab.org/exp_prog/proposals/proposal_updates/PR12-09-019_pac35.pdf (2008).
- ⁴⁸³ [20] E. B. Hughes, T. A. Griffy, M. R. Yearian, and R. Hofstadter, *Phys. Rev.* **139**, B458 (1965).
- ⁴⁸⁴ [21] R. G. Arnold *et al.*, *Phys. Rev. Lett.* **61**, 806 (1988).
- ⁴⁸⁵ [22] L. Durand, *Phys. Rev.* **115**, 1020 (1959).
- ⁴⁸⁶ [23] E. E. W. Bruins *et al.*, *Phys. Rev. Lett.* **75**, 21 (1995).
- ⁴⁸⁷ [24] G. Kubon *et al.*, *Phys. Lett.* **B524**, 26 (2002), arXiv:nucl-ex/0107016 [nucl-ex].
- ⁴⁸⁸ [25] J. Lachniet *et al.* (CLAS), *Phys. Rev. Lett.* **102**, 192001 (2009), arXiv:0811.1716 [nucl-ex].
- ⁴⁸⁹ [26] V. Punjabi, C. F. Perdrisat, M. K. Jones, E. J. Brash, and C. E. Carlson, *Eur. Phys. J.* **A51**, 79 (2015), arXiv:1503.01452 [nucl-ex].
- ⁴⁹¹ [27] A. Puckett, unpublished. See https://hallaweb.jlab.org/wiki/index.php/Documentation_of_g4sbs (2016).
- ⁴⁹³ [28] D. E. Wiser, “Photoproduction of protons, kaons and pions at slac energies,” Ph.D. thesis, University of Wisconsin (1977).